PHYSICAL REVIEW B VOLUME 4, NUMBER 4 15 AUGUST 1971

Measurement and Inversion of de Haas-van Alphen Data in Gold†

B. Bosacchi,* J. B. Ketterson, and L. R. Windmiller
Argonne National Laboratory, Argonne, Illinois 60439
(Received 22 March 1971)

We have studied the extremal areas and cyclotron effective masses in gold using the de Haas–van Alphen effect. The experimental data have been inverted to obtain the Fermi radius and velocity at any point of the Fermi surface. The inversion techniques are described and some results on other quantities of experimental interest are also presented.

I. INTRODUCTION

The de Haas–van Alphen (dHvA) effect, as one of the most powerful tools in the study of the Fermi surface of metals, has been extensively used.[1] The main emphasis, however, has been on the frequencies F_i of the oscillations which are directly related to the extremal cross-sectional areas A_i of the surface by the relation[2]

$$F_i = (\hbar c/2\pi e)A_i \ , \tag{1a}$$

where i denotes the ith cross-sectional area. Much less effort has been expended to date on studying the cyclotron effective masses m_i^*, where

$$m_i^* = \frac{1}{2\pi}\frac{\partial A_i}{\partial E} \ . \tag{1b}$$

The cyclotron effective mass follows from studying the temperature dependence of the amplitude of the dHvA oscillations. Actually m^* is measured more directly by means of the Azbel-Kaner microwave cyclotron resonance experiments. We argue, however, that the dHvA method is at least as effective for the following reasons: (a) The accuracy obtainable in the dHvA and microwave methods is about the same; (b) the microwave method requires much purer samples with specially prepared surfaces; (c) the phase of the oscillations is much larger in the dHvA case and thus the measured mass corresponds more closely to the extremal orbit; and (d) for orbits of low symmetry, the orbits of extremal m_i^* and extremal A_i may be different, and thus our knowledge of the positions of the orbit plane is less certain in the microwave case.

Precise studies of the cyclotron effective mass are particularly interesting at the present time. Techniques for computing the shape of the Fermi surface from band structure are now quite well developed. However, for energies near the Fermi energy, various many-body effects reduce the value of the Fermi velocity $\partial E/\partial\vec{k}$ from that calculated from the band structure. These velocity shifts appear to lie outside the present range of calculational competence. Thus, the cyclotron effective mass, which involves an orbital average of the Fermi velocity, is an interesting object of study. Effective-mass data are fairly complete in the other noble metals Ag and Cu[3–7] as well as the near-noble metals Pt and Pd,[8,9] whereas the Au data are less satisfactory.[10–12] Thus, one object of the present study was to obtain better data on cyclotron masses in Au. Since spin-orbit coupling effects are important in the heavy transition metals and thus larger g shifts are expected, a better knowledge of the effective mass is also useful for obtaining g factors from the harmonic content of the dHvA effect.[13,14] The gold effective-mass data obtained in the present study are presented in Sec. II of this paper.

The other object of the present study was to develop and apply more powerful inversion schemes, based on the Fourier-series representation,[15–17] for converting dHvA areas $A_i(\theta, \varphi)$ and cyclotron effective masses $m_i^*(\theta, \varphi)$ into Fermi radii $k(\theta, \varphi)$ and velocities $\vec{v}_F(\theta, \varphi)$. A scheme for obtaining the pressure derivatives of the surface from the pressure dependence of the dHvA areas has been given previously,[18] and a similar one to get the relaxation time at any point from the Dingle-Robinson temperature of some dHvA orbits has also been developed.[19] In Sec. III we present the various inversion procedures, while in Sec. IV we apply these techniques to gold.

II. EXPERIMENTAL

The single crystal used in the present investigation had the shape of a cylinder, about 1 mm in diameter and $\frac{1}{4}$ in. long, and was obtained by using zone-stretching and air-annealing techniques already described elsewhere.[20,21] Starting from a wire of pure gold (99.9999% pure and $\frac{1}{16}$ in. in diameter[22]), we obtained a sample with a residual resistance ratio of 1600 which could be oriented such that the magnetic field rotated approximately in a (110) plane. The precise orientation of the sample is specified by four angles which we have defined previously,[8,23] the values being given by $\theta_1 = 33°$, $\varphi_1 = 41°$, $\theta_2 = 90°$, $\varphi_2 = 43°$, $\alpha = 90°$, and $\Psi_0 = 32$. These values have an uncertainty of approximately ± ½°. The dHvA apparatus and the various techniques which we have used for enhancing specific frequencies have also been described in detail.[24,25] For conditions such that B-H effects may be neglected (well satisfied in this experiment) the magnetization is given by[13]

$$\vec{\mathrm{M}}_i = \hat{M}_i \left(\frac{e}{hc}\right)^{1/2} \left[\frac{A_i k_B T}{\pi H^{1/2}} \left(\frac{\partial^2 A_i}{\partial k_\perp^2}\right)^{1/2}\right]$$

$$\times \left(\frac{e^{-2\pi^2 c k_B T_x m_i^*/\hbar e H}}{\sinh(2\pi^2 c k_B T m_i^*/\hbar e H)}\right)$$

$$\times \sin\left(\frac{2\pi F_i}{H} + \beta_i\right) \cos\left(\frac{\hbar g_i m_i^*}{2 m_0}\right) , \qquad (2)$$

where the vector direction of the magnetization is given by

$$\hat{M}_i = \hat{H} + \frac{1}{A_i} \frac{\partial A_i}{\partial \theta} \hat{\theta} + \frac{1}{A_i \sin\theta} \frac{\partial A_i}{\partial \varphi} \hat{\varphi} .$$

Here, we have the Dingle-Robinson scattering temperature T_x, the orbital g factor g_i, and the phase β_i. Using (2) we may also study the scattering temperature T_x from the field dependence of the amplitude (once m^* is known), the g factor from the harmonic content[14] [not included in Eq. (2)], and $\partial^2 A_i / \partial k_\perp^2$ from the absolute amplitude.[26] The cyclotron effective mass follows from a plot of $\ln(M/H)$ vs T, where the slope is given by $m^*/(6.806 H \times 10^{-6})$. The slope was in all cases determined by least-squares fitting to no less than five measurements of the dHvA amplitude in the temperature range 0.9–1.7 K. The temperature was determined from the vapor pressure of the ^{4}He bath surrounding the sample using a Texas Instruments precision pressure gauge.[27] Cooling of the sample bath was accomplished with a second pumped ^{4}He bath which was in thermal equilibrium with the sample bath. Since the sample bath is static, no pressure-drop corrections are necessary. (The sample bath was connected to room temperature via a 1-in. tube and thus no thermomolecular-pressure-head corrections are necessary.) The average error of the measurements is estimated at less than 1%. Our investigation in a plane near (110) allowed a determination of all five symmetry-point-centered orbits in a single run: [100] and [111] bellies, neck, four-cornered rosette, and dogs'-bone orbits in the nomenclature of Shoenberg.[10] We denote these orbits as B_{100}, B_{111}, N, R, and D, respectively.

Our areas, as a function of the direction of $\hat{H}$ in the experimental plane, are shown in Fig. 1. The angular dependence was determined with high accuracy using the field-rotation technique. The absolute values of the frequencies are known with less accuracy and the data of Fig. 1 were normalized to agree with the absolute values reported by Schirber and O'Sullivan[28] [after correcting for the fact that the sample plane is slightly removed from the (110) plane] since the latter were measured with an NMR calibrated magnetic field. The Schirber and O'Sullivan[28] data are in excellent agreement with the less complete data of Jan and Templeton.[29] In addition to the data of Fig. 1, we have observed frequencies for the field near [211] corresponding to extended belly orbits connected by one, two, and three necks. An unsuccessful effort was made to find the six-cornered rosette for the field near [111].

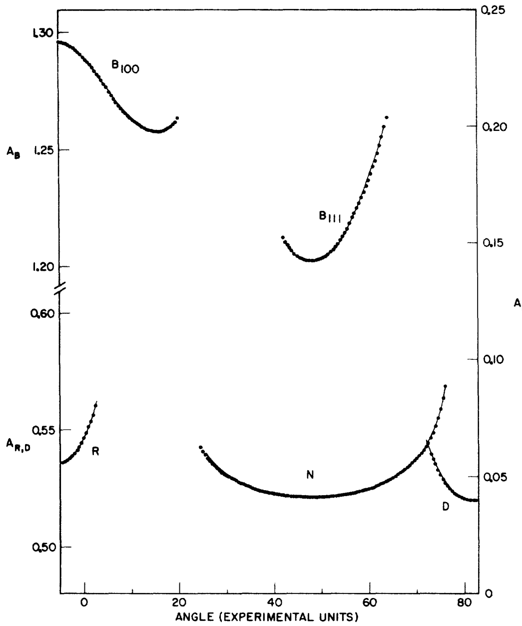

FIG. 1. Angular variation of the dHvA areas (in a.u.) in the experimental plane. Dots are experimental points; the continuous curve is calculated in the $R8$ representation. The angular scale on the abscissa refers to experimental units and is such that a change of 10 in the coordinate corresponds to a change in angle of 10.37°. (Note the different scales for A_B, A_R, A_D, and A_N.)

The experimental cyclotron effective masses are reported in Fig. 2. The accuracy of the data was sharply dependent on the region; whereas in some cases the values reported are well reproducible and probably highly accurate (error ≲ 1%), a much larger error (> 2%) is present for the B_{111} masses.

III. COMPUTATIONAL TECHNIQUES

The extremal areas and the related cyclotron effective masses, as given by the dHvA effect, must be inverted in order to get the radii and the velocities at any point of the Fermi surface. For closed sheets, powerful techniques have been de-

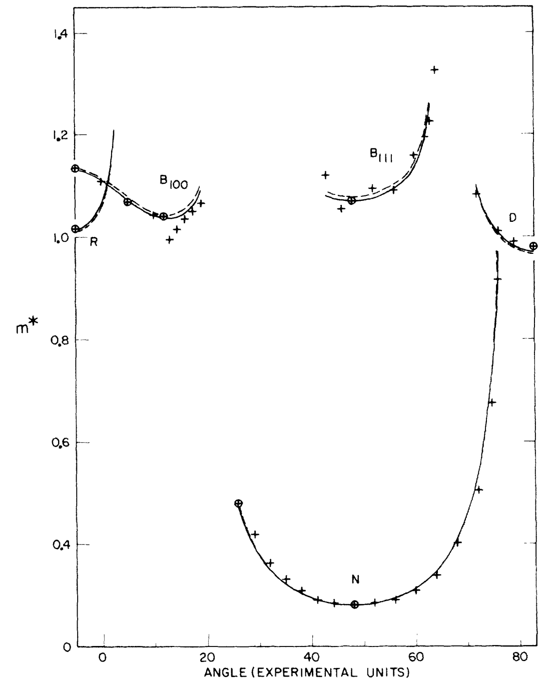

FIG. 2. Angular variation of the effective masses (in electron masses) in the experimental plane. Dots are experimental points; encircled dots are the points chosen for the fit of Table III. Continuous and dashed curves are calculated in the $R8$ representation, with the coefficients of Table III, without and with the density-of-states constraint, respectively. The angular scale on the abscissa refers to experimental units and is such that a change of 10 in the coordinate corresponds to a change in angle of 10.37°.

veloped which have been discussed in detail elsewhere.[30-32] For open sheets, a convenient way to achieve the inversion is based on the Fourier-series representation of the Fermi surface which has already been used with success for the noble metals by Roaf[15] and by Halse[16]; recently, in an improved version, it has been shown to work well even for more distorted surfaces, like the open sheets in Pd and Pt.[8,9,17] We now discuss the analytic and numerical techniques which will be used to perform the inversions of the area and effective-mass data using the Fourier-series representation.

We use the following implicit equation as our representation of the Fermi surface:

$$F(\vec{k}) = \sum_{\vec{R}} C_{\vec{R}} e^{i\vec{k}\cdot\vec{R}} = 0 \,, \tag{3}$$

where the $\vec{R}$'s are the position vectors of the real-space Bravais lattice. $F(\vec{k})$ must transform as the identity representation and, furthermore, have inversion symmetry. Since these vectors may be factored into sets or "stars" which are invariant under the operations of the point group, we rewrite Eq. (3) as a summation over these stars:

$$F(\vec{k}) = \textstyle\sum_j C_j S_j(\vec{k}) \,, \tag{4}$$

with

$$S_j(k) = \sum_{\substack{\text{all } \vec{R} \text{ in} \\ j\text{th star}}} e^{i\vec{k}\cdot\vec{R}} \,. \tag{5}$$

In Eqs. (4) and (5), j indexes stars associated with vectors of increasing length.

The inversion from areas to radii has already been described in detail,[17] and we need only to recall the main points and to report some minor modifications. Let us assume we have some set of C_j of representation (4); a general orbit described by an electron in the magnetic field $\vec{H}$ is defined by the intersection of the Fermi surface with a plane $\vec{k}\cdot\hat{H} = k_{\parallel}$, where $\vec{k}$ is the electron coordinate in the momentum space and $k_{\parallel}$ is its component along $\hat{H}$. Writing

$$\vec{k}(E_F) = k_{\parallel}\hat{H} + \vec{k}_{\perp} \,, \tag{6}$$

the area of the orbit is given by

$$A^c = \tfrac{1}{2}\int_0^{2\pi} k_{\perp}^2(\theta)\, d\theta \,, \tag{7}$$

θ being the angle in the plane of the orbit of $\vec{k}_{\perp}$ with respect to some convenient reference axis. From Eq. (7), using the law of differentiation of implicit functions, one derives the following expressions for other quantities of interest:

$$\frac{\partial A^c}{\partial C_j} = -\int_0^{2\pi} \frac{k_{\perp}^2}{\vec{k}_{\perp}\cdot\vec{\nabla}F} S_j(\vec{k})\, d\theta \,, \tag{8}$$

$$\frac{\partial A^c}{\partial k_{\parallel}} = -\int_0^{2\pi} \frac{k_{\perp}^2}{\vec{k}_{\perp}\cdot\vec{\nabla}F} (\hat{H}\cdot\vec{\nabla}F)\, d\theta \,, \tag{9}$$

$$\frac{\partial^2 A^c}{\partial k_{\parallel}^2} = \int_0^{2\pi} \left(\frac{\vec{k}_{\perp}}{\vec{k}_{\perp}\cdot\vec{\nabla}F}\right)^2 [\hat{H}\cdot\vec{\nabla}F)^2 - (\vec{k}_{\perp}\cdot\vec{\nabla}F)(\hat{H}\cdot\vec{\nabla}\vec{\nabla}F\cdot\hat{H}) + (\hat{H}\cdot\vec{\nabla}F)(\hat{H}\cdot\vec{\nabla}\vec{\nabla}F\cdot\vec{k}_{\perp})]\, d\theta \,, \tag{10}$$

where we need expressions for $\vec{\nabla}F$ and $\vec{\nabla}\vec{\nabla}F$ which are clearly given by

$$\vec{\nabla}F = i\sum_{\vec{R}} \vec{R}\, C_{\vec{R}}\, e^{i\vec{k}\cdot\vec{R}} \,, \tag{11}$$

$$\vec{\nabla}\vec{\nabla}F = -\sum_{\vec{R}} \vec{R}\vec{R}\, C_{\vec{R}}\, e^{i\vec{k}\cdot\vec{R}} \,. \tag{12}$$

The quantities calculated in Eq. (8) are of central importance in our inversion schemes; as we shall see they come in both the area and mass inversions; they have also been used to invert the pressure-dependence data for the Fermi surfaces of the noble metals.[18] Equation (9) is important in the discussion of helicon and magnetoacoustic experiments,[33] where the phenomena of the Doppler-shifted cyclotron resonance are encountered. The value of $\partial A/\partial k_{\parallel}$ at the limiting point (at which $k_{\parallel}$ crosses the Fermi surface) gives the Gaussian curvature. At the limiting point the numerator and denominator in the integrand of Eq. (9) vanish and an asymptotic expression is required. We have derived the following equation to handle this case:

$$\left(\frac{\partial A^c}{\partial k_\parallel}\right)_{\mathrm{lim}} = 2\pi \left|\vec{\nabla} F\right| \left[(\hat{n}_2 \cdot \vec{\nabla}\vec{\nabla} F \cdot \hat{n}_2)(\hat{n}_3 \cdot \vec{\nabla}\vec{\nabla} F \cdot \hat{n}_3) - (\hat{n}_2 \cdot \vec{\nabla}\vec{\nabla} F \cdot \hat{n}_3)^2\right]^{-1/2} \quad (13)$$

where $\hat{n}_2$ and $\hat{n}_3$ are any two mutually perpendicular unit vectors which are in turn perpendicular to the surface normal $\hat{n}_1$. A suitable set of vectors is given by

$$\hat{n}_1 = \frac{\vec{\nabla} F}{|\vec{\nabla} F|}, \quad \hat{n}_2 = \frac{\vec{k} \times \hat{n}_1}{|\vec{k} \times \hat{n}_1|}, \quad \hat{n}_3 = \hat{n}_1 \times \hat{n}_2 . \quad (14)$$

Equation (10) appears in the expression for the amplitude of the dHvA oscillations.[13] The integrals (7)–(10) are evaluated by means of the Simpson rule carried out by using the "return to surface" and "stepping" routines discussed previously.[17] Here, we have improved the "return to surface" procedure, by executing it in a quadratic approximation: We start from the second-order Taylor expansion to relate the energy corresponding to the trial starting vector $\vec{k}$ and the new one $\vec{k} = \vec{k} + \delta\vec{k} = (\vec{k}_\perp + \delta\vec{k}_\perp) + \vec{k}_\parallel$:

$$F(\vec{k} + \delta\vec{k}) \cong F(\vec{k}) + \vec{\nabla} F \cdot \delta\vec{k}_\perp + \tfrac{1}{2}\, \delta\vec{k}_\perp \cdot \vec{\nabla}\vec{\nabla} F \cdot \delta\vec{k}_\perp \quad (15)$$

and, since according to Eq. (4), $F(\vec{k} + \delta\vec{k}) = 0$, we return to the surface by replacing $\vec{k}$ with

$$\vec{k}' = \vec{k} + \vec{k}_\perp \frac{-\vec{k}_\perp \cdot \vec{\nabla} F + [(\vec{k}_\perp \cdot \vec{\nabla} F)^2 - 2F(\vec{k})\, \vec{k}_\perp \cdot \vec{\nabla}\vec{\nabla} F \circ \vec{k}_\perp]^{1/2}}{\vec{k}_\perp \cdot \vec{\nabla}\vec{\nabla} F \circ \vec{k}_\perp} . \quad (16)$$

We have seen above how to study the geometrical properties of the Fermi surface by starting from a given set of $\{C\}$. The optimal coefficients are determined through a variational procedure, which minimizes the rms error,

$$\Delta^2(\{C\}) = \frac{1}{N} \sum_{i=1}^{N} \frac{(A_i^c - A_i)^2}{A_i^2} \quad (17)$$

between a set of N experimental areas A_i and the corresponding A_i^c calculated with Eq. (7). We expand the calculated area in a Taylor series through second order:

$$A_i^c(\{C + \delta C\}) = A_i^c(\{C\}) + \sum_j \frac{\partial A_i^c}{\partial C_j}\, \delta C_j + \frac{1}{2} \sum_{j,k} \frac{\partial^2 A_i^c}{\partial C_j\, \partial C_k}\, \delta C_j\, \delta C_k . \quad (18)$$

Inserting Eq. (18) in Eq. (17) and minimizing with respect to $\{\delta C\}$ while again retaining only terms through second order we obtain for the nth equation,

$$\frac{2}{N} \sum_i \frac{A_i^c - A_i}{A_i^2} \frac{\partial A_i^c}{\partial C_n} + \frac{2}{N} \sum_{i,k} \frac{1}{A_i^2} \frac{\partial A_i^c}{\partial C_n} \frac{\partial A_i^c}{\partial C_k}\, \delta C_k + \frac{2}{N} \sum_{i,k} \frac{A_i^c - A_i}{A_i^2} \frac{\partial^2 A_i^c}{\partial C_n\, \partial C_k}\, \delta C_k + \frac{1}{N} \sum_{i,k,l} \frac{1}{A_i^2} \left(\frac{\partial A_i^c}{\partial C_n} \frac{\partial^2 A_i^c}{\partial C_k\, \partial C_l} + 2\, \frac{\partial A_i^c}{\partial C_k} \frac{\partial^2 A_i^c}{\partial C_n\, \partial C_l} \right) \delta C_k\, \delta C_l = 0 , \quad (19)$$

where $\partial A_i^c / \partial A$ has already been given in Eq. (8) and $\partial^2 A_i^c / \partial C_j \partial C_l$ is given by

$$\frac{\partial^2 A_i^c}{\partial C_j\, \partial C_l} = \int_0^{2\pi} \frac{k_\perp^2}{(\vec{k}_\perp \cdot \vec{\nabla} F)^2} \left(S_j(\vec{k})\, S_l(\vec{k}) + S_j(\vec{k})\, \vec{k}_\perp \cdot \vec{\nabla} S_l(\vec{k}) + S_l(\vec{k}) \vec{k}_\perp \circ \vec{\nabla} S_j(\vec{k}) - \frac{S_j(\vec{k})\, S_l(\vec{k}) \vec{k}_\perp \cdot \vec{\nabla}\vec{\nabla} F \cdot \vec{k}_\perp}{\vec{k}_\perp \cdot \vec{\nabla} F} \right) d\theta . \quad (20)$$

Retaining the first two terms in Eq. (19) corresponds to a linear least-squares fit, while inclusion of the last two corresponds to quadratic accuracy; for the remainder of this paper we will restrict ourselves to a linear least-squares fit. We now define the vector

$$X_j = \frac{2}{N} \sum_i \frac{A_i^c - A_i}{A_i^2} \frac{\partial A_i^c}{\partial C_j} \quad (21)$$

and matrix

$$T_{jl} = \frac{2}{N} \sum_i \frac{1}{A_i^2} \frac{\partial A_i^c}{\partial C_j} \frac{\partial A_i^c}{\partial C_l} . \quad (22)$$

With these definitions and restrictions, Eq. (19) reads

$$X_j + \sum_l T_{jl}\, \delta C_l = 0 , \quad (23)$$

which is easily solved using matrix-inversion techniques. We wish to perform our minimization, however, with the constraint that the total number of carriers is such that there is one electron in the first Brillouin zone as expected for the case of Au. The volume V of the Fermi surface is given by

$$V(\{C\}) = \int A(k_\parallel, \{C\})\, dk_\parallel . \quad (24)$$

(The analogous expression in spherical coordinates is given in Appendix D.) Let V_0 be one-half the volume of the first zone. We want to minimize Eq. (17) with the constraint $V(\{C\}) = V_0$, and this yields

$$X_j + \sum_l T_{jl}\,\delta C_l + \lambda \frac{\partial V}{\partial C_j} = 0 , \tag{25}$$

where λ is a Lagrange multiplier, which is found to be given by

$$\lambda = \left(V(\{C\}) - V_0 - \sum_{m,n} (T^{-1})_{mn} \frac{\partial V}{\partial C_m} X_n \right) \Bigg/ \sum_{m,n} (T^{-1})_{m,n} \frac{\partial V}{\partial C_m} \frac{\partial V}{\partial C_n} , \tag{26}$$

$$\frac{\partial V}{\partial C_j} = \int \frac{\partial A(k_{\parallel}, \{C\})}{\partial C_j}\, dk_{\parallel} . \tag{27}$$

With these expressions we may calculate a new set $\{C\}$ which more accurately minimizes Eq. (17). It is useful to have an expression for the predicted rms error, that is, the error we would expect if we use the new set of coefficients $\{C + \delta C\}$. This is easily shown to be

$$\Delta^2(\{C + \delta C\}) = \Delta^2(\{C\}) + \tfrac{1}{2} \textstyle\sum_j X_j\, \delta C_j , \tag{28}$$

and this expression is useful in deciding when to stop the iteration procedure.

We now discuss the cyclotron effective-mass inversion. Since $\sum C_j S_j(\vec{k})$ does not, in general, represent the band structure in the vicinity of E_F, $\vec{\nabla} F$ will be different from the Fermi velocity $\vec{v}_F = \vec{\nabla} E$ although $\vec{v}_F$, being perpendicular to the surface, will be parallel to $\vec{\nabla} F$. We shall, however, introduce a new set of coefficients $\{C'\}$ and write the velocity in the following way, which satisfies the symmetry requirements:

$$\vec{v}_F = \vec{\nabla} E = - \vec{\nabla} F / \textstyle\sum C'_j S_j(\vec{k}) . \tag{29}$$

Equation (29) may be derived by considering the coefficients $C_j(E)$ of Eq. (4) as energy dependent. The velocity then follows from considering the surface at $E + dE$ for which the expansion coefficients are $C_j(E + dE) = C_j(E) + C'_j(E)\, dE$. Solutions of Eq. (4) for $E + dE$ yield values of $\vec{k} + d\vec{k}$ and thus we can compute the velocity $\vec{v} = dE/d\vec{k}$. Alternatively, we could look for a unique set of coefficients which fits simultaneously the area and cyclotron effective-mass data; this more general inversion scheme, in which both $\vec{k}_F$ and $\vec{v}_F$ are derived from a single function $E(\vec{k})$, is discussed in Appendix A.

The cyclotron effective mass is given (in a.u.) by

$$m^c = \frac{1}{\pi} \frac{\partial A^c}{\partial E} . \tag{30}$$

By differentiating Eq. (7) with respect to E we have

$$\frac{\partial A^c}{\partial E} = \int_0^{2\pi} \frac{k_\perp^2}{\vec{k}_\perp \cdot \vec{\nabla} E}\, d\theta \tag{31}$$

and, from Eq. (29),

$$\frac{\partial A^c}{\partial E} = - \sum C'_j \int \frac{k_\perp^2 S_j(\vec{k})}{\vec{k}_\perp \cdot \vec{\nabla} F}\, d\theta . \tag{32}$$

Finally, from Eq. (8), we get

$$\frac{\partial A^c}{\partial E} = \sum_j C'_j \frac{\partial A^c}{\partial C_j} . \tag{33}$$

Since $\partial A / \partial C_j$ for a given orbit and $S_j(\vec{k})$ for a given point may be considered known quantities from the above discussion, a knowledge of the $\{C'\}$ coefficients enables us to get, through Eqs. (29) and (33), the velocity at any point and the cyclotron effective mass for any orbit we wish; it will give us also the density of states [see Eq. (45)]. The $\{C'\}$ coefficients are obtained from the experiments by defining, in analogy with Eq. (17), a new function

$$D^2(\{C'\}) = \frac{1}{M} \sum_{i=1}^{M} \left(\frac{\partial A_i^c}{\partial E} - \frac{\partial A_i}{\partial E} \right)^2 \Bigg/ \left(\frac{\partial A_i}{\partial E} \right)^2 \tag{34}$$

and by varying the $\{C'\}$ until the best fit is obtained to the set of M experimental masses m_i. Again, the minimization of D^2 can be carried out either without any constraint, or imposing the condition that the density of states $N(E)$ [calculated using Eqs. (43) and (44)] be equal to the value obtained experimentally through specific-heat measurements.[34] (We shall discuss in Sec. IV the meaning of this procedure.)

Without the density-of-states constraint the minimization of Eq. (34) leads to the equations

$$\sum_i \left(\frac{\partial A_i}{\partial E} \right)^{-2} \left(\frac{\partial A_i^c}{\partial E} - \frac{\partial A_i}{\partial E} \right) \frac{\partial^2 A_i^c}{\partial E\, \partial C'_j} = 0 , \tag{35}$$

which, with the use of Eq. (33), becomes

$$- \sum_i \left(\frac{\partial A_i}{\partial E} \right)^{-1} \frac{\partial A_i^c}{\partial C_j} + \sum_{il} \left(\frac{\partial A_i}{\partial E} \right)^{-2} \frac{\partial A_i^c}{\partial C_j} \frac{\partial A_i^c}{\partial C_l} C'_l = 0 . \tag{36}$$

Defining the vector

$$Y_j = - \sum_i \left(\frac{\partial A_i}{\partial E} \right)^{-1} \frac{\partial A_i^c}{\partial C_j} \tag{37}$$

and the matrix

$$U_{jl} = \sum_i \left(\frac{\partial A_i}{\partial E} \right)^{-2} \frac{\partial A_i^c}{\partial C_j} \frac{\partial A_i^c}{\partial C_l} , \tag{38}$$

we can rewrite Eq. (36) in the compact form

$$Y_j + \textstyle\sum_l U_{jl} C'_l = 0 . \tag{39}$$

With the density-of-states constraint on the coefficients the situation is completely analogous to that considered in Eqs. (25) and (26) and Eq. (39) changes to

$$Y_j + \lambda \frac{\partial V}{\partial C_j} + \sum_l U_{jl} C'_l = 0 , \tag{40}$$

from which we get

$$C_i' = -\sum_j (U^{-1})_{ij}\left(Y_j + \lambda \frac{\partial V}{\partial C_j}\right) , \tag{41}$$

where λ is found to be

$$\lambda = -\left(\sum_{nm} (U^{-1})_{nm} Y_m \frac{\partial V}{\partial C_n} + \frac{\partial V_0}{\partial E}\right)\Bigg/\sum_{nm} (U^{-1})_{nm} \frac{\partial V}{\partial C_n}\frac{\partial V}{\partial C_m} . \tag{42}$$

The final point is the calculation of the density of states at the Fermi energy, which is straightforward once the $\{C'\}$ coefficients are known. In fact, we have

$$N(E) = \frac{2}{(2\pi)^3}\frac{\partial V}{\partial E} = \frac{2}{(2\pi)^3}\int \frac{\partial A(k_\parallel)}{\partial E}\, dk_\parallel \tag{43}$$

and, from Eq. (30),

$$N(E) = \frac{1}{(2\pi)^2}\int m^*(k_\parallel)\, dk_\parallel . \tag{44}$$

(The analogous expression in spherical coordinates is given in Appendix D.) Since m^* is given by Eq. (33), the integral in Eq. (44) may be simply evaluated simultaneously with Eq. (24). More simply, however, using Eq. (33) and Eq. (27) we can write

$$N(E) = \frac{2}{(2\pi)^3}\sum_j C_j' \frac{\partial V}{\partial C_j} , \tag{45}$$

which gives directly the density of states in terms of $\{C'\}$. In conclusion, we have seen in this section how, starting from a set of N experimental areas and M experimental cyclotron effective masses, we can derive a set of coefficients $\{C\}$ and $\{C'\}$, which enables us to get the volume and the density of states of the Fermi surface, the area, the cyclotron effective mass, the derivatives of the area with respect to $k_\parallel$ for any orbit, and the Fermi radii and the Fermi velocities for any point of the surface. The above scheme, though similar to that of Halse, has the advantage of compactness, completeness, and rapid convergence over that of Halse.[16] In particular, for the calculation of the cyclotron effective masses and of the density of states, we do not need to pass through the properties of the surface of energy $E_F + dE$, but we use directly our knowledge of the differential properties of the Fermi surface. The above scheme will be applied in Sec. IV to the case of gold.

TABLE I. Experimental and calculated values for the main extremal dHvA areas expressed in a.u.

Orbit	Experimental area	Calculated area with the $R8$ representation
B_{100}	1.2964	1.2964
B_{111}	1.2015	1.2008
R	0.5354	0.5353
D	0.5180	0.5180
N	0.0410	0.0410
B[22° in the (110) plane]	1.2571	1.2574
B[16.2° in the (100) plane]	1.2753	1.2751

TABLE II. Coefficients of Halse and our representations, with the error with which the experimental areas of Table II are fitted.

	Halse	$R5$	$R6$	$R8$
C_1	1.000000	1.000000	1.000000	1.000000
C_2	4.028360	0.796434	4.028360	4.028360
C_3	−1.340230	0.212169	−1.202660	−1.340230
C_4	−2.528120	−0.013567	−2.384670	−2.400300
C_5	−0.399370	0.046049	−0.357621	−0.233042
C_6	−0.511763	···	−0.391843	−0.618918
C_7	···	···	···	0.118184
C_8	···	···	···	0.198816
Error	0.279%	0.262%	0.205%	0.026%

IV. RESULTS OF THE CALCULATIONS

The values of the areas used in Eq. (17) are listed in Table I. These seven values were selected because they are extremal with respect to changes in the direction of the magnetic field and are thus insensitive to a misalignment of the crystal. For those areas for which the magnetic field lies along a symmetry axis (the first five in Table I) we used the values obtained by Schirber and O'Sullivan,[28] since the magnetic field was measured with NMR and thus the accuracy is expected to be quite high. The remaining two areas were taken from Halse[16] (B_{22}) and Joseph *et al.*[12] (B_{16}) but were corrected to agree with the value for B_{100} of Schirber and O'Sullivan.[28]

As discussed in Appendix B, the matrix T resulting from a six-star fit was nearly singular. This suggests that a good fit can be obtained using only five stars; Table II lists the coefficients of the resulting five-star representation $R5$. Nonetheless, the rms error does decrease for fits including a larger number of stars, although the coefficients in Eq. (4) tend to become larger with each succeeding iteration (a result of the singular character of T). It was observed that a small rms error could be obtained while at the same time avoiding a singular matrix if one or more additional coefficients were held constant [in addition to C_1 which is set equal to 1, since we may always divide Eq. (4) by C_1], i.e., by decreasing the size of the matrix and eliminating a nearly dependent equation. Table II lists the coefficients of a six-star representation $R6$ obtained when C_1 and C_2 were held constant. Shown for comparison is the six-star representation of Halse. In order to obtain a nonsingular matrix for an eight-star fit it proved necessary to keep the values of C_1, C_2, and C_3 constant. The rms error of the various fits is also listed in Table II. The eight-star representation $R8$ is seen to have a very small rms error and furthermore gives a very good over-all fit to the data. For this reason we have performed all our remaining calculations using the eight-star representation.

The continuous curve in Fig. 1 shows the calculated angular variation of the dHvA areas for H varying in the experimental plane (defined as in Sec. II). The agreement with the experimental points is quite close. The only discrepancy is the fact that some experimental points have been observed slightly beyond the direction where, according to the representation, the extremal orbits should cut off. This is a minor point, however, very likely due to a small inaccuracy in the assumed orientation of our experimental plane; alternatively, it may be due to the finite width of the "belt" of electrons which contribute to the dHvA effect. The volume of the surface was found to contain one electron per atom (within experimental or calculational error) for all three of our representations. This verifies the assumption that the volume of the Fermi surface is not affected by many-body interactions; this assumption is central to Fermi-liquid theory. (Fits made with the volume constraint give negligibly different results.) The above calculation provides also the coefficients $\partial A/\partial C_j$ of the areas for which the cyclotron effective masses have been studied; the mass inversion, through Eq. (39), is therefore straightforward.

TABLE III. Coefficients C'_j as obtained in the $R8$ representation, without and with the constraint on the value of the density of state.

	(a) Without constraint	(b) With constraint
C'_1	0.0	0.0
C'_2	0.0	0.0
C'_3	−82.4586	25.8263
C'_4	−70.8485	59.6772
C'_5	−16.8915	49.1934
C'_6	−14.7248	45.8113
C'_7	12.1088	51.2581
C'_8	6.958 52	18.3477

The only problem is the choice of the set of masses to be fitted, which has some arbitrariness; one could, of course, take all the experimental data and get the best fit to all of them. But, in view of the very different accuracy of the results for the different regions of the Fermi surface, some sort of weighting would have to be introduced. We have preferred to weight equally all points used in the fit, and to eliminate entirely the less reliable values. The circled dots in Fig. 2 are the values selected for the fit. For the set of $\{C'\}$ coefficients so determined, the angular variation of the cyclotron effective mass m^* in the experimental plane has also been plotted in Fig. 2. The inversion procedure has been performed both with and without the constraint that the density of states, calculated through Eq. (45), be equal to the experimental value deduced from specific-heat measurements.[34]

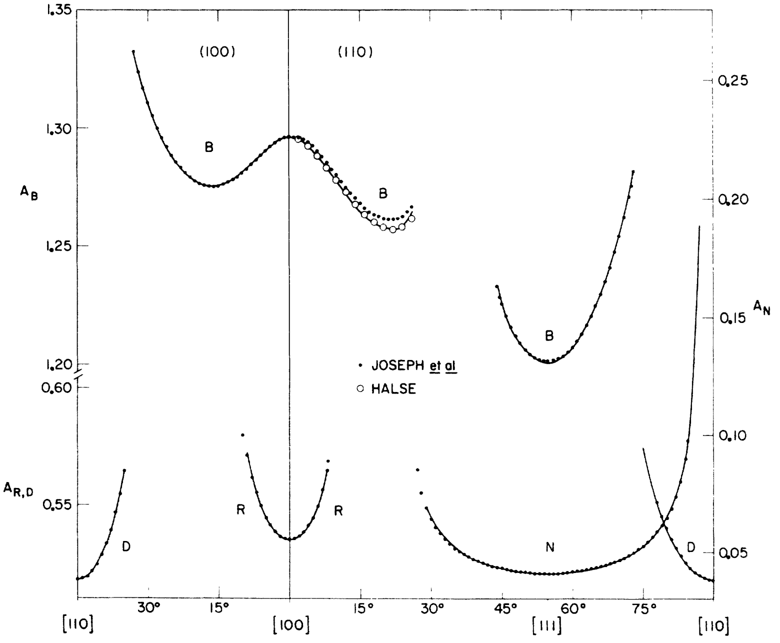

FIG. 3. Angular variation of the dHvA areas (in a.u.) in the (100) and (110) planes. The continuous curve is calculated in the $R8$ representation; also shown for comparison are the experimental data of Joseph *et al.* (Ref. 12) (dots) and Halse (Ref. 16) (open circles). (Note the different scales for A_B, A_R, A_D, and A_N.)

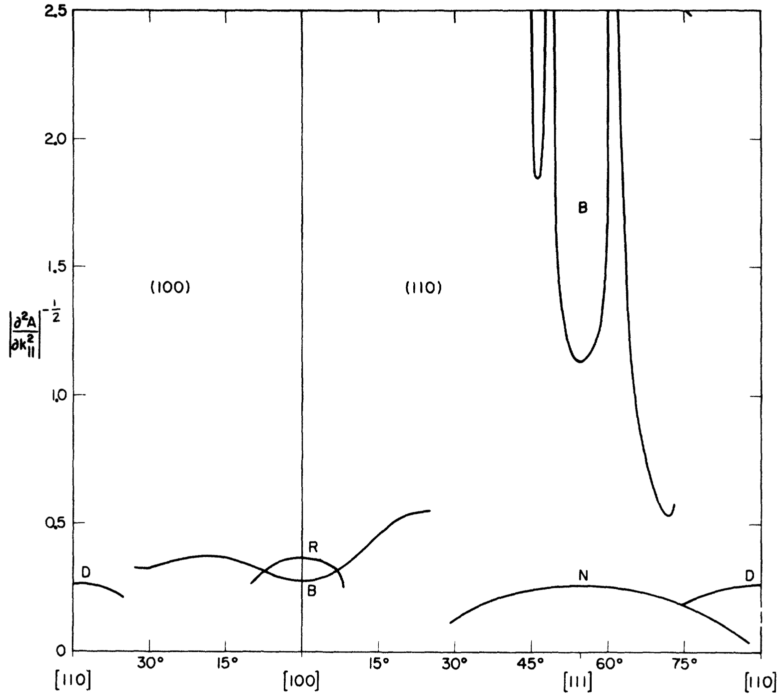

FIG. 4. Angular variation of amplitude factor $(\partial^2 A/\partial k_\parallel^2)^{-1/2}$ in the (100) and (110) planes, as calculated in the $R8$ representation.

The techniques for performing the volume and density-of-states integrations are discussed in Appendix D. The two resulting curves (dashed and continuous, respectively) are shown in Fig. 2. Table III lists the expansion coefficients for the eight-star fits with and without the density-of-states constraint. Note that the first two coefficients have been set equal to 0. The first coefficient was equated to 0, because a surface at $E+\Delta E$ can also be described by $C_1(E+\Delta E)=1$ which results in $C_1'(E)=0$. The second was set equal to 0 because a nearly singular matrix U results otherwise. The

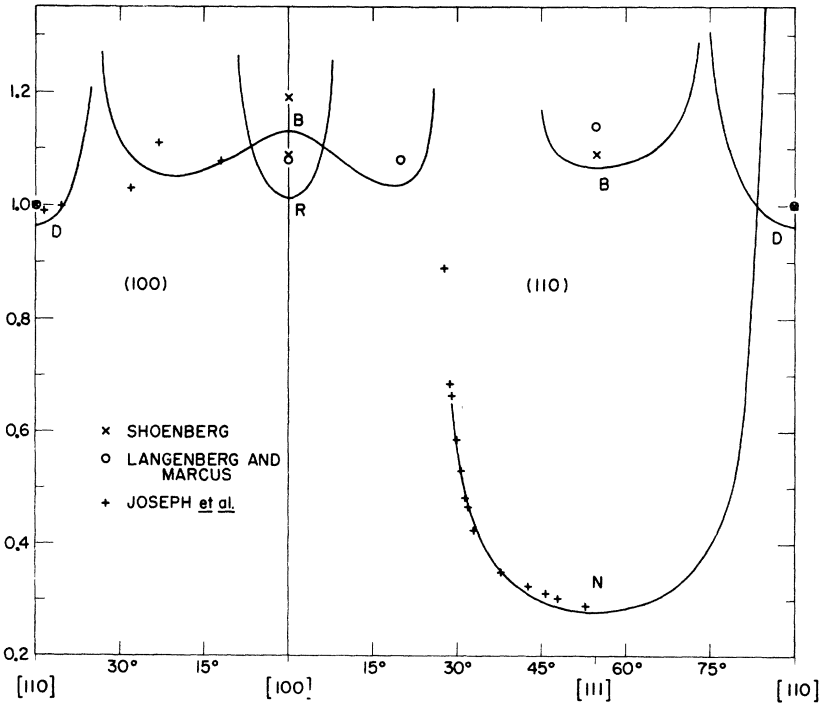

FIG. 5. Angular variation of the cyclotron effective masses (in electron masses) in the (100) and (110) planes. The continuous curve is calculated in the $R8$ representation with the $\{C'\}$ coefficients of Table III without the density-of-states constraint. Also shown for comparison are the experimental data of Shoenberg (Ref. 10), ×; Langenberg and Marcus (Ref. 11), O; and Joseph *et al.* (Ref. 12), +.

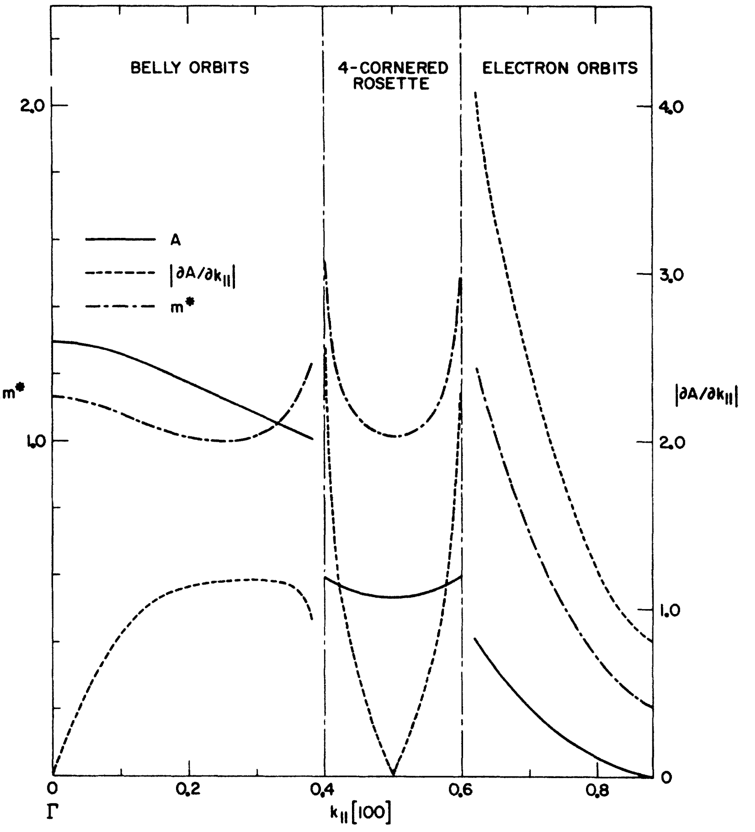

FIG. 6. Areas, $\partial A/\partial k_\parallel$, and m^* as a function of $k_\parallel$ in the [100] direction. (Scale of the ordinate is in atomic and electron mass units; that of the abscissa in units such that the distance $\Gamma - X$ in the Brillouin zone is equal to 1.)

constraint on the density of states is justified by the Landau theory of a Fermi liquid which predicts that the effect of the many-body interactions are taken into account by a renormalization of the effective mass. From a knowledge of the variation of the cyclotron effective mass over the Fermi surface, one can derive the density of states through Eq. (44), and one has, in principle, a way to test the above conclusion. For the fit of Fig. 2, the density of states calculated without constraint is lower by 0.8% than that corresponding to the experimental value of Martin.[34] In view of the large inaccuracy of our results in the B_{111} region, and of the fact that the belly electrons are just those which most heavily contribute to the density of states, we must conclude that, within the limit of the experimental error, the two values coincide. In the calculations which follow, the density-of-states constraint has not been included. Thus, we are taking the point of view that our measurements provide an independent determination of the electronic heat capacity of Au. Since errors of order 1% are not uncommon in heat-capacity work this may be a reasonable point of view. We find the value $\gamma = 163.78$ μcal K^{-2} mole^{-1}.

With the representation for the Fermi radius and Fermi velocity reported above, we have done

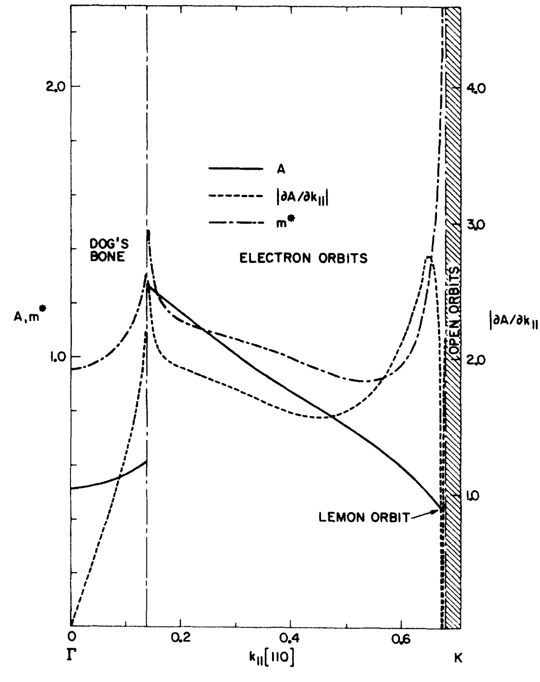

FIG. 7. Areas, $\partial A/\partial k_\parallel$, and m^* as a function of $k_\parallel$ in the [110] direction. (Scale of the ordinate is in atomic and electron mass units; that of the abscissa in units such that the distance $\Gamma - X$ in the Brillouin zone is equal to 1.)

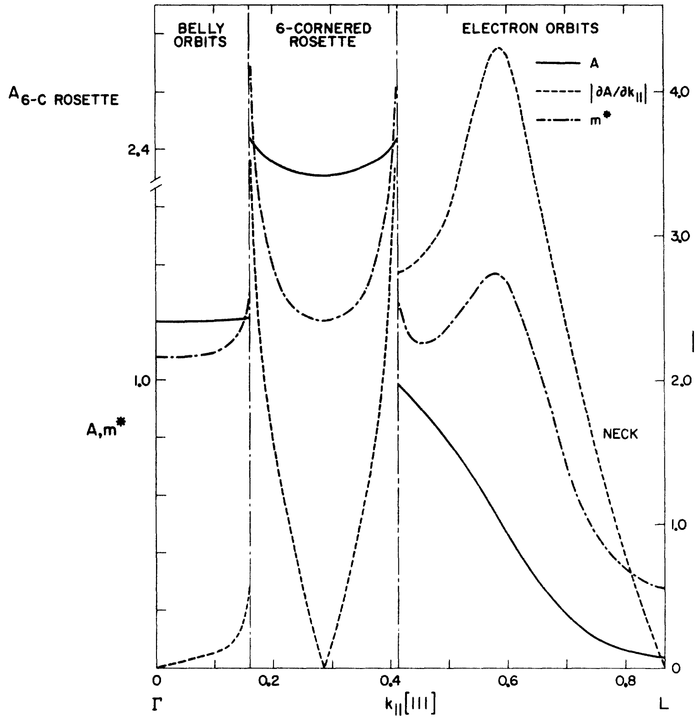

FIG. 8. Areas, $\partial A/\partial k_{\parallel}$, and m^* as a function of $k_{\parallel}$ in the [111] direction. (The scale of the ordinate is in atomic and electron mass units; that of the abscissa in units such that the distance $\Gamma - X$ in the Brillouin zone is equal to 1.)

an extensive study of various quantities of experimental interest. Part of the results are shown in Figs. 3–9. Figure 3 shows the calculated angular variation of the dHvA areas as $\hat{H}$ varies in the (100) and (110) planes. A portion of the available experimental data are also shown in Fig. 3. The data of Joseph *et al.* have been corrected to agree with the NMR measured values of Schirber and O'Sullivan at the symmetry direction. For $\hat{H}$ near [100] in the (110) plane, there is a considerable difference between the result of Halse and those of Joseph *et al.* Halse has argued that this must be due to a sample misorientation in the work of Joseph *et al.* since the belly area must be an absolute minimum for $\hat{H}$ near the minimum at 22° from [100]. A point to be noted is that the rosette orbit, for the directions of the field out of the (110) plane, is not necessarily centered at *W*; this point

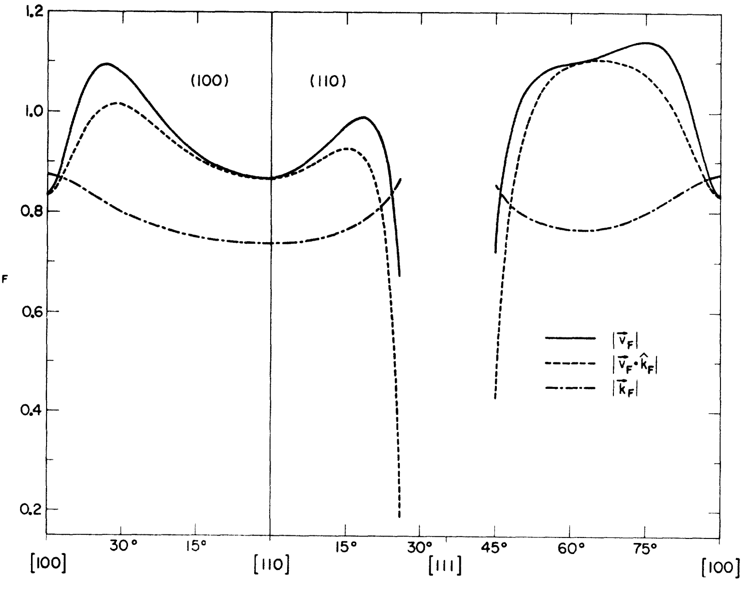

FIG. 9. Angular dependence of $|\vec{v}_F|$, $|\hat{k}_F \cdot \vec{v}_F|$, and $|\vec{k}_F|$ for the (100) and (110) planes. (Scale on the ordinate is in units such that the distance $\Gamma - X$ in the Brillouin zone is equal to 1.)

has been discussed elsewhere,[17] and must be accounted for in calculating the theoretical curve.

Figure 4 shows the angular variation of $[\partial^2 A/\partial k_\parallel^2]^{-1/2}$, for the dHvA areas with $\hat{H}$ in the (110) and (100) planes. This quantity appears in the expression for the amplitude of the dHvA oscillations [see Eq. (2)]; no comparison with experimental values is possible at present, since these measurements, which are very difficult, are still in a preliminary stage.[26] A striking feature of Fig. 4 is the vanishing of $\partial^2 A/\partial k_\parallel^2$ near [111]; this is discussed in Appendix C.

Figure 5 reports the angular variation of the cyclotron effective mass in the planes (100) and (110), as calculated from the set of coefficients in Table III(a). Also reported in the figure are the experimental results presently available.[10–12] Good agreement is found in the neck region, whereas in the other regions the data are too inaccurate or incomplete to allow a meaningful comparison. Figures 6–8 give the variation of the area, the derivative of the area with respect to $k_\parallel$, and the cyclotron effective mass, as a function of $k_\parallel$, for $k_\parallel$ in the [100], [110], and [111] directions, respectively. Note in the [110] direction (Fig. 7) and in the [111] direction (Fig. 8), the prediction of a "lemon" orbit, and of a "six-cornered rosette" orbit, analogous to those found by Halse for Cu. We have been unable to find the six-cornered rosette experimentally; since it is nearly twice the B_{111} area it is probably obscured by the belly second harmonic. We are not aware of any experimental measurements of extreme values of $\partial A/\partial k_\parallel$ in gold although our results are qualitatively similar to those in copper, where experimental data do exist.[35] The variation with $k_\parallel$ of the cyclotron effective mass also has some interest; according to our calculations the cyclotron effective mass has several extremal values, in addition to those related to the extremal dHvA areas. Since in cyclotron resonance experiments extremal masses are observed, the presence of these subsidiary extremals may complicate the interpretation of the experiments; it may be that in many cases it is difficult to resolve the different values, which are predicted to be rather close. In any case, it does not seem that this aspect of the problem has been taken into account so far in the interpretation of the Asbel-Kaner cyclotron resonance (AKCR) results. In Fig. 9 is reported the Fermi velocity, without the density-of-states constraint, along the intersection of the surface with the (100) and (110) planes. The anisotropy of the Fermi velocity is qualitatively analogous to that found for the other noble metals.[16]

V. CONCLUSIONS

We have developed and applied here some improved methods for obtaining Fermi radii and Fermi velocities from dHvA areas and cyclotron effective masses based on Fourier-series representations. An eight-term series is found to give an exceptionally good fit to the available dHvA areas and thus should give an accurate representation of the shape of the Fermi surface. The volume of the surface obtained contains one conduction electron per atom within experimental error. A second eight-term expansion is obtained which when combined with the first expansion gives a good overall fit to the available cyclotron effective-mass data and thus yields a representation of the Fermi velocity. The resulting density of states is found to agree with the value obtained in electronic specific-heat measurements within experimental error. This result is in agreement with present many-body theory which predicts that the total density of states (measured by the electronic heat capacity) and the quasiparticle density of states (computed using the cyclotron mass) should be identical.

ACKNOWLEDGMENTS

We would like to thank J. Shaw for preparing the single crystal used in this investigation and G. Crabtree for assistance in performing the measurements.

APPENDIX A

For some purposes it may be useful to develop a single function $E(\vec{k})$ from which both the Fermi radius and Fermi velocity may be deduced. The Fermi surface follows from the solution of $E(\vec{k}) = E_F$ (where E_F is arbitrary) and the Fermi velocity is given by $\vec{v} = \vec{\nabla}_k E(\vec{k})$. We now describe a procedure for finding $E(\vec{k})$ from a set of measured dHvA areas and effective masses. We again define $E(\vec{k})$ by

$$E(\vec{k}) = \textstyle\sum_j C_j S_j(\vec{k}) \ , \tag{A1}$$

and note that $\partial A^c/\partial E$ is given by

$$\frac{\partial A^c}{\partial E} \doteq \int_0^{2\pi} \frac{k_\perp^2}{\vec{k}_\perp \cdot \vec{\nabla} E} \ . \tag{A2}$$

We employ the following more general error function:

$$\Delta^2 = \frac{1-x}{N} \sum_{i=1}^{N} \left(\frac{A_i^c - A_i}{A_i} \right)^2 + \frac{x}{M} \sum_{i=1}^{M} \left[\left(\frac{\partial A_i^c}{\partial E} - \frac{\partial A_i}{\partial E} \right) \Big/ \frac{\partial A_i}{\partial E} \right]^2 \ , \tag{A3}$$

where N and M are the number of experimental areas and effective masses, respectively, and x is a weighting factor which accounts for the fact that the effective-mass data usually have less accuracy ($x = 0$ would correspond to zero statistical weight for the mass data). We require the following expansions:

$$A_i^c(\{C+\delta C\}) = A_i^c(\{C\}) + \sum_j \frac{\partial A_i}{\partial C_j}\,\delta C_j \ , \tag{A4}$$

$$\frac{\partial A_i^c}{\partial E}(\{C+\delta C\}) = \frac{\partial A_i^c}{\partial E}(\{C\}) + \sum_j \frac{\partial^2 A_i}{\partial C_j\,\partial E}\,\delta C_j \ , \tag{A5}$$

where

$$\frac{\partial A}{\partial C_j} = -\int_0^{2\pi} \frac{k_\perp^2 S_j(\vec{k})}{(\vec{k}_\perp\cdot\vec{\nabla}E)}\,d\theta \ , \tag{A6}$$

$$\frac{\partial^2 A}{\partial C_j\,\partial E} = \int_0^{2\pi}\left(-\frac{k_\perp^2 S_j(\vec{k})}{(\vec{k}_\perp\cdot\vec{\nabla}E)^2} + \frac{k_\perp^2 S_j(\vec{k})\vec{k}_\perp\cdot\vec{\nabla}\vec{\nabla}E\cdot\vec{k}_\perp}{(\vec{k}_\perp\cdot\vec{\nabla}E)^3} - \frac{k_\perp^2\vec{k}_\perp\cdot\vec{\nabla}S_j(\vec{k})}{(\vec{k}_\perp\cdot\vec{\nabla}E)^2}\right)d\theta \ . \tag{A7}$$

Inserting Eqs. (A4) and (A5) in Eq. (A3) and minimizing with respect to δC_j we obtain

$$X_j + \textstyle\sum_l T_{jl}\,\delta C_l = 0 \ , \tag{A8}$$

where

$$X_j = \frac{1-x}{N}\sum_i \frac{A_i^c - A_i}{A_i^2}\,\frac{\partial A_i^c}{\partial C_j} + \frac{x}{M}\sum_i\left[\left(\frac{\partial A_i^c}{\partial E} - \frac{\partial A_i}{\partial E}\right)\Big/\left(\frac{\partial A_i}{\partial E}\right)^2\right]\frac{\partial^2 A_i^c}{\partial C_j\,\partial E} \ , \tag{A9}$$

$$T_{jl} = \frac{1-x}{N}\sum_i \frac{1}{A_i^2}\,\frac{\partial A_i^c}{\partial C_j}\,\frac{\partial A_i^c}{\partial C_l} + \frac{x}{M}\sum_i\left(\frac{\partial A_i}{\partial E}\right)^{-2}\frac{\partial^2 A_i^c}{\partial C_j\,\partial E}\,\frac{\partial^2 A_i^c}{\partial C_l\,\partial E} \ . \tag{A10}$$

If we wish to include the number of carriers and density-of-states constraints

$$V^c(\{C+\delta C\}) \cong V^c(\{C\}) + \sum_j \frac{\partial V^c}{\partial C_j}\,\delta C_j = V_0 \ , \tag{A11}$$

$$\frac{\partial V^c}{\partial E}(\{C+\delta C\}) \cong \frac{\partial V^c(\{C\})}{\partial E} + \sum_j \frac{\partial^2 V^c}{\partial C_j\,\partial E}\,\delta C_j = \frac{\partial V_0}{\partial E} \ , \tag{A12}$$

then Eq. (A8) becomes

$$X_j + \lambda_1\frac{\partial V^c}{\partial C_j} + \lambda_2\frac{\partial^2 V^c}{\partial C_j\,\partial E} + \sum_l T_{jl}\,\delta C_l = 0 \ . \tag{A13}$$

Requiring that Eqs. (A11) and (A12) be satisfied we find the following for λ_1 and λ_2:

$$\lambda_1 = \left[\left(\frac{\partial^2 V^c}{\partial E\,\partial\vec{C}}\cdot\overleftrightarrow{T}^{-1}\cdot\frac{\partial^2 V}{\partial E\,\partial\vec{C}}\right)\left(V^c - V_0 - \frac{\partial V^c}{\partial\vec{C}}\cdot\overleftrightarrow{T}^{-1}\cdot\vec{X}\right) - \left(\frac{\partial V^c}{\partial\vec{C}}\cdot\overleftrightarrow{T}^{-1}\cdot\frac{\partial^2 V^c}{\partial E\,\partial\vec{C}}\right)\left(\frac{\partial V^c}{\partial E} - \frac{\partial V_0}{\partial E} - \frac{\partial^2 V}{\partial E\,\partial\vec{C}}\cdot\overleftrightarrow{T}^{-1}\cdot\vec{X}\right)\right] \Big/ \left[\left(\frac{\partial V^c}{\partial\vec{C}}\cdot\overleftrightarrow{T}^{-1}\cdot\frac{\partial V^c}{\partial\vec{C}}\right)\left(\frac{\partial^2 V^c}{\partial E\,\partial\vec{C}}\cdot\overleftrightarrow{T}^{-1}\cdot\frac{\partial^2 V^c}{\partial E\,\partial\vec{C}}\right) - \left(\frac{\partial V^c}{\partial\vec{C}}\cdot\overleftrightarrow{T}^{-1}\cdot\frac{\partial^2 V^c}{\partial E\,\partial\vec{C}}\right)^2\right] , \tag{A14}$$

$$\lambda_2 = \left[-\left(\frac{\partial V^c}{\partial\vec{C}}\cdot\overleftrightarrow{T}^{-1}\cdot\frac{\partial^2 V^c}{\partial E\,\partial\vec{C}}\right)\left(V^c - V_0 - \frac{\partial V^c}{\partial\vec{C}}\cdot\overleftrightarrow{T}^{-1}\cdot\vec{X}\right) + \left(\frac{\partial V^c}{\partial\vec{C}}\cdot\overleftrightarrow{T}^{-1}\cdot\frac{\partial V^c}{\partial\vec{C}}\right)\left(\frac{\partial V^c}{\partial E} - \frac{\partial V_0}{\partial E} - \frac{\partial^2 V}{\partial E\,\partial\vec{C}}\cdot\overleftrightarrow{T}^{-1}\cdot\vec{X}\right)\right] \Big/ \left[\left(\frac{\partial V^c}{\partial\vec{C}}\cdot\overleftrightarrow{T}^{-1}\cdot\frac{\partial V^c}{\partial\vec{C}}\right)\left(\frac{\partial^2 V^c}{\partial E\,\partial\vec{C}}\cdot\overleftrightarrow{T}^{-1}\cdot\frac{\partial^2 V^c}{\partial E\,\partial\vec{C}}\right) - \left(\frac{\partial V^c}{\partial\vec{C}}\cdot\overleftrightarrow{T}^{-1}\cdot\frac{\partial^2 V^c}{\partial E\,\partial\vec{C}}\right)^2\right] . \tag{A15}$$

APPENDIX B

In attempting to improve Halse's six-star fit for Au it was observed that the resulting matrix T was quite singular (here we did not vary C_1 so the matrix was really a 5×5). Since a singular matrix implies that at least one of the equations is linearly dependent we conclude that an equally good fit can be had using only a five-star fit. To test this point we developed a program for performing a least-squares fit to a set of radii; this program is, in effect, a simplification of the corresponding one described in Sec. III for fitting areas. We calculated 40 radii, in the basic $\frac{1}{48}$th of the unit sphere, using the Halse coefficients. We then performed a least-squares fit to these radii holding C_6 constant while varying C_2 through C_5 until Δ^2 minimized. Figure 10 shows the rms error Δ as a function of C_6; shown also are the coefficients C_2 through C_5. We observe that C_2 through C_5 are nearly linearly dependent on C_6 and that Δ rises to ~ 0.1% on setting C_6 equal to 0. With the limited set of accurate area data (i.e., points measured where the area is an extremum as a function of the magnetic field direction) we do not have sufficient sensitivity to determine C_6 and thus we have set it equal to 0. A nearly singular matrix was also encountered when we attempted to obtain a better fit by extending the expansion to include C_7 or C_8 in the fit (still setting $C_6=0$). To demonstrate that the Halse fits for Cu and Ag do not differ substantially from those of Au we have shown his values of C_2 through C_6 for Cu, Ag, and Au in Fig. 10; observe that they fall quite close to the Au coefficient contours. This situation is expected since the Cu, Ag, and Au surfaces are quite similar.

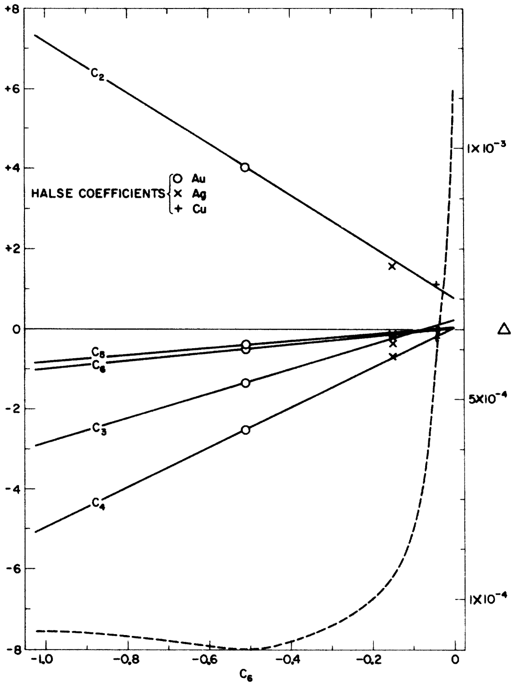

FIG. 10. Values of the coefficients C_2 through C_6 which minimize Δ^2 as a function of C_6. Shown also is the value of Δ as a function of C_6 (dashed curve) and the coefficients of the Halse representations for the Fermi surface of Cu, +; Ag, ×; and Au, O.

APPENDIX C

A striking feature of Fig. 4 is the vanishing of $\partial^2 A/dk_\parallel^2$ near [111]. This would seemingly imply through Eq. (2) an infinite amplitude for the dHvA oscillations. This anomaly is caused by the particular expansion used to calculate the dHvA amplitude; higher-order terms become important in the limit as $\partial^2 A/dk_\parallel^2$ approaches 0 and Eq. (2) is no longer valid.

The dHvA amplitude is calculated by assuming that the Fermi surface is divided into slices of thickness $dk_\parallel$ by planes normal to the magnetic field direction $\hat{k}_\parallel$. Then each slice will contribute a component to the oscillatory magnetization with a frequency characteristic of the value of the cross-sectional area of the Fermi surface in the plane of the slice:

$$M(k_\parallel) = A \sin[2\pi F(k_\parallel)/H] \ . \tag{C1}$$

Then the resultant magnetization will be given by

$$M = A \int_{-\infty}^{+\infty} \sin[2\pi F(k_\parallel)/H] dk_\parallel \ . \tag{C2}$$

Since the phase of the oscillations is usually very high this integral does not converge unless $F(k_\parallel)$ has a stationary nonzero value for some $k_\parallel$. Measuring $k_\parallel$ from this point we can expand $F(k_\parallel)$ in a Taylor series:

$$F(k_\parallel) = F(0) + \frac{1}{2}\frac{\partial^2 F}{\partial k_\parallel^2} k_\parallel^2 + \frac{1}{6}\frac{\partial^3 F}{\partial k_\parallel^3} k_\parallel^3 + \frac{1}{24}\frac{\partial^4 F}{\partial k_\parallel^4} k_\parallel^4 \ . \tag{C3}$$

In the usual case only the first term in the expansion is retained, leading to

$$M = A \int_{-\infty}^{+\infty} \left[\sin\frac{2\pi F(0)}{H} \cos\left(\frac{\pi}{H}\frac{\partial^2 F}{\partial k_\parallel^2} k_\parallel^2\right) + \cos\frac{2\pi F(0)}{H} \sin\left(\frac{\pi}{H}\frac{\partial^2 F}{\partial k_\parallel^2} k_\parallel^2\right)\right] dk_\parallel$$

$$= \frac{AH^{1/2}}{2} \left|\frac{\partial^2 F}{\partial k_\parallel^2}\right|^{-1/2} \sin\left(\frac{2\pi F(0)}{H} + \frac{\pi}{4}\operatorname{sgn}\frac{\partial^2 A}{\partial k_\parallel^2}\right) . \tag{C4}$$

However, if $\partial^2 F/\partial k_\parallel^2$ vanishes then the next term in the expansion must be used in the integral of Eq. (C2). For stationary frequencies associated with planes of high symmetry only even orders of $k_\parallel^n$ can appear in Eq. (C3) and so the leading term will be the $n = 4$ term. For this case, we have

$$M = A \int_{-\infty}^{+\infty} \left[\sin\frac{2\pi F(0)}{H} \cos\left(\frac{\pi}{12H}\frac{\partial^4 F}{\partial k_\parallel^4} k_\parallel^4\right) + \cos\frac{2\pi F(0)}{H} \sin\left(\frac{\pi}{12H}\frac{\partial^4 F}{\partial k_\parallel^4} k_\parallel^4\right)\right] dk_\parallel$$

$$= \frac{A}{2}\left(\frac{12H}{\pi}\right)^{1/4} \left|\frac{\partial^4 F}{\partial k_\parallel^4}\right|^{-1/4} \Gamma(\tfrac{1}{4}) \sin\left(\frac{2\pi F(0)}{H} + \frac{\pi}{8}\operatorname{sgn}\frac{\partial^4 A}{\partial k_\parallel^4}\right) . \tag{C5}$$

Equation (C5) has three important differences from Eq. (C4). First, the amplitude is determined by $\partial^4 F/\partial k_\parallel^4$ rather than $\partial^2 F/\partial k_\parallel^2$. Second, the magnetic field dependence of the dHvA amplitude is different in the two cases. Dingle-Robinson temperatures are derived from the field dependence of the dHvA amplitude and care must be used when applying the usual formulas in regions where $\partial^2 F/\partial k_\parallel^2$ is small. Third, the dHvA phase correction is different for the two cases.

Finally, there may be rare cases when the leading term in the expansion (C3) is the $n = 3$ term. This would correspond to a stationary value of the frequency rather than an extremum. In that case the dHvA amplitude is given by

$$M = \tfrac{2}{3} A \left(\frac{3H}{\pi}\right)^{1/3} \left(\frac{\partial^3 F}{\partial k_\parallel^3}\right)^{-1/3} \Gamma(\tfrac{1}{3}) \cos\frac{\pi}{6} \sin\left(\frac{2\pi F(0)}{H}\right) . \tag{C6}$$

Note in this case the different magnetic field dependence of the amplitude and the absence of the dHvA phase correction.

APPENDIX D

Here, we discuss very briefly the techniques used to perform the volume and density-of-states calculations. Rather than Eqs. (24), (27), and (48), which are given in cylindrical coordinates, the actual calculations were performed in spherical coordinates. The analogous expressions in spherical coordinates are

$$V=\tfrac{1}{3}\int k^3 \sin\theta \, d\theta \, d\varphi \ , \tag{D1}$$

$$\frac{\partial V}{\partial C_j}=-\int \frac{k^2}{\hat{k}\cdot\vec{\nabla}F} S_j(\vec{k}) \sin\theta \, d\theta \, d\varphi \ , \tag{D2}$$

$$\frac{\partial V}{\partial E}=\int \frac{k^2}{\hat{k}\cdot\vec{\nabla}E} \sin\theta \, d\theta \, d\varphi \ , \tag{D3}$$

where k, θ, and φ are the usual spherical coordinates. The integrations were confined to the basic $\frac{1}{48}$th wedge $k_x > k_y > k_z$. For maximum accuracy the integrations were performed using Simpson's rule doing the θ sums first followed by the sum over φ (the integration initiated at the intersection of the neck and the L plane with $\varphi = 45°$). In the course of carrying out these sums two procedures are required. When we are on the intersection of the neck with the L plane we need a routine to advance along the neck to a specified angle φ. The simultaneous solution of the following three equations yields a vector $\vec{\delta k}$ by which we correct $\vec{k}$ to converge to the neck and the desired value of φ:

$$F(\vec{k}+\vec{\delta k}) \cong F(\vec{k}) + \vec{\nabla}F\cdot \vec{\delta k} = 0 \ , \tag{D4a}$$

$$\hat{n}\cdot(\vec{k}+\vec{\delta k}) = k_{\Gamma L} \ , \tag{D4b}$$

$$(\vec{k}+\vec{\delta k})\cdot\hat{x}\tan\varphi = (\vec{k}+\vec{\delta k})\cdot\hat{y} \ , \tag{D4c}$$

where $\hat{n}$ is a unit vector in the [111] direction and $k_{\Gamma L}$ is the distance from Γ to L. When we are not on the neck intersection we require a routine to advance to a specified value of θ and φ. The solution of the following three equations yields a value of $\vec{\delta k}$ by which we correct $\vec{k}$ to converge on the desired values of θ and φ:

$$F(\vec{k}+\vec{\delta k}) \cong F(\vec{k}) + \vec{\nabla}F\cdot \vec{\delta k} = 0 \ , \tag{D5a}$$

$$(\vec{k}+\vec{\delta k})\cdot\hat{y} = \tan\varphi(\vec{k}+\vec{\delta k})\cdot\hat{x} \ , \tag{D5b}$$

$$(\vec{k}+\vec{\delta k})\cdot\hat{y} = \tan\theta \, \sin\varphi(\vec{k}+\vec{\delta k})\circ\hat{z} \ . \tag{D5c}$$

The values of θ and φ which lie on the $k_z = k_y$ corner of the wedge are related by $\sin\theta\sin\varphi = \cos\theta$. In addition to integrating over the values of θ and φ which lie on the surface, the volume integral must include the volume enclosed by the intersection of the surface with the L plane. This contribution is easily seen to be given by $\frac{1}{3}A^{\text{neck}}k_{\Gamma L}$.

---

†Based on work performed under the auspices of the U.S. Atomic Energy Commission.

*On leave from the Istituto de Fisica, Gruppo Nazionale di Struttura della Materia del C.N.R., Parma, Italy.

[1] See, for a recent and comprehensive review, A. V. Gold, *Electrons in Metals*, Vol. I of *Solid State Physics*, edited by J. F. Cochran and R. R. Haering (Gordon and Breach, New York, 1968), p. 39.

[2] L. Onsager, Phil. Mag. 43, 1006 (1952).

[3] A. S. Joseph and A. C. Thorsen, Phys. Rev. 138, A1159 (1965).

[4] D. H. Howard, Phys. Rev. 140, 1705 (1965).

[5] J. F. Koch, R. A. Stradling, and A. F. Kip, Phys. Rev. 133, A240 (1964).

[6] A. S. Joseph, A. C. Thorsen, A. C. Gertner, and L. E. Valby, Phys. Rev. 148, 569 (1966).

[7] D. A. Smith, Proc. Roy. Soc. (London) A297, 205 (1967).

[8] J. B. Ketterson and L. R. Windmiller, Phys. Rev. B 2, 4813 (1970).

[9] J. B. Ketterson and L. R. Windmiller Phys. Rev. B 3, 4213 (1971).

[10] D. Shoenberg, Phil. Trans. Roy. Soc. London A255, 85 (1962).

[11] D. N. Langenberg and S. M. Marcus, Phys. Rev. 136, A1383 (1964).

[12] A. S. Joseph, A. C. Thorsen, and F. A. Blum, Phys. Rev. 140, A2046 (1965).

[13] I. M. Lifshitz and A. M. Kosevich, Zh. Eksperim. i Teor. Fiz. 29, 730 (1955) [Sov. Phys. JETP 2, 636 (1956)].

[14] D. Randles (unpublished).

[15] D. J. Roaf, Phil. Trans. Roy. Soc. London A255, 135 (1962).

[16] M. R. Halse, Phil. Trans. Roy. Soc. London A265, 507 (1969).

[17] J. B. Ketterson, F. M. Mueller, and L. R. Windmiller, Phys. Rev. 186, 656 (1969).

[18] B. Bosacchi, J. B. Ketterson, and L. R. Windmiller, Phys. Rev. B 2, 3025 (1970).

[19] J. B. Ketterson, B. Bosacchi, and L. R. Windmiller, Bull. Am. Phys. Soc. 16, 336 (1971).

[20] J. B. Ketterson, J. S. Tait, and L. R. Windmiller, J. Cryst. Growth 1, 323 (1967).

[21] S. Hornfeldt, J. B. Ketterson, and L. R. Windmiller, J. Cryst. Growth 5, 289 (1969).

[22] Sigmund Cohn Corp., Mt. Vernon, N. Y.

[23] F. M. Mueller, J. B. Ketterson, and L. R. Windmiller, J. Appl. Phys. 41, 2312 (1970).

[24] R. W. Stark and L. R. Windmiller, Cryogenics 8, 272 (1968).

[25] L. R. Windmiller and J. B. Ketterson, Rev. Sci. Instr. 39, 1672 (1968).

[26] D. Shoenberg and L. R. Vanderkooy, J. Low Temp. Phys. 2, 483 (1970).

[27] Texas Instruments Inc., Houston, Tex.

[28] J. E. Schirber and W. J. O'Sullivan, Colloq. Intern. Centre Natl. Rech. Sci. (Paris) 118, 113 (1970); Phys. Rev. B 1, 1443 (1970).

[29] J. P. Jan and I. M. Templeton, Phys. Rev. 161, 556 (1967).

[30] I. M. Lifshitz and A. V. Pogorelov, Dokl. Akad. Nauk SSSR 96, 1143 (1954).

[31] F. M. Mueller, Phys. Rev. 148, 636 (1966).

[32] J. B. Ketterson and L. R. Windmiller, Phys. Rev. B 1, 463 (1970); R. Aurbach, J. B. Ketterson, and L. R. Windmiller, Proceedings of the Conference on the Physics of Semimetals and Narrow Gap Semiconductors, Dallas, 1970 (unpublished).

[33] Y. Eckstein, Phys. Letters 20, 142 (1966); 20, 606 (1966); J. A. Munarin, Phys. Rev. 172, 737 (1968); H. N. Spector, Solid State Phys. 19, 291 (1966).

[34] D. L. Martin, Phys. Rev. 170, 650 (1968).

[35] See, e.g., B. Perrin, G. Weisbuch, and A. Libchaber, Phys. Rev. B 1, 1501 (1970); L. T. Wood and J. D. Gavenda, *ibid.* 2, 1492 (1970).